

GenUDC: High Quality 3D Mesh Generation with Unsigned Dual Contouring Representation

Ruowei Wang
Sichuan University
Chengdu, China
wangruowei1027@gmail.com

Jiaqi Li
Sichuan University
Chengdu, China
2023226040007@stu.scu.edu.cn

Dan Zeng
Southern University of Science and
Technology
Shenzhen, China
zengd@sustech.edu.cn

Xueqi Ma
Shenzhen University
Shenzhen, China
qixuemaa@gmail.com

Zixiang Xu
Sichuan University
Chengdu, China
xzx34@stu.scu.edu.cn

Jianwei Zhang
Sichuan University
Chengdu, China
zhangjianwei@scu.edu.cn

Qijun Zhao*
Sichuan University
Chengdu, China
qjzhao@scu.edu.cn

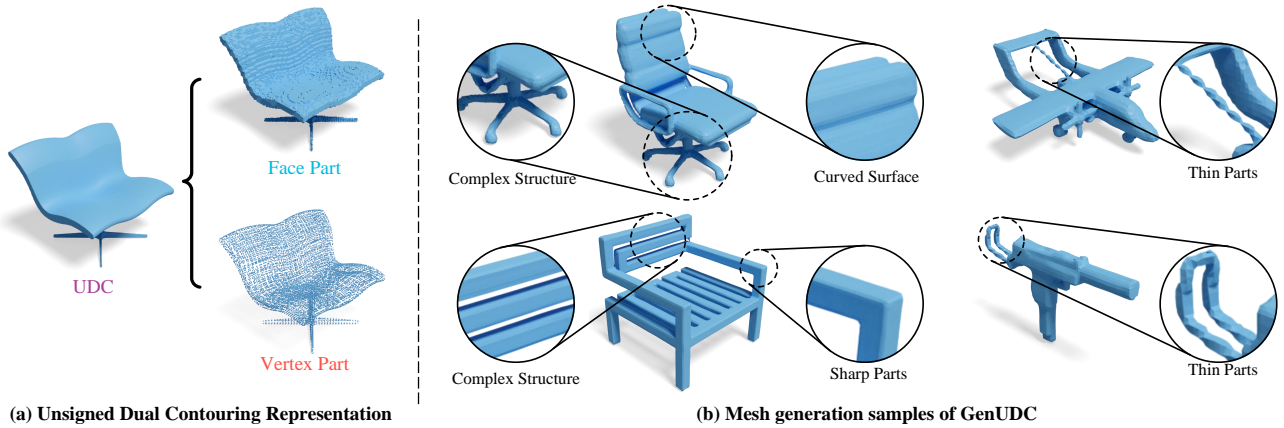


Figure 1: (a) A visual sample of Unsigned Dual Contouring Representation (UDC) consisting of the face part and vertex part. (b) Our high-quality mesh generation results in 64³ resolution with close-up views.

Abstract

Generating high-quality meshes with complex structures and realistic surfaces is the primary goal of 3D generative models. Existing methods typically employ sequence data or deformable tetrahedral grids for mesh generation. However, sequence-based methods have difficulty producing complex structures with many faces due

to memory limits. The deformable tetrahedral grid-based method MeshDiffusion fails to recover realistic surfaces due to the inherent ambiguity in deformable grids. We propose the GenUDC framework to address these challenges by leveraging the Unsigned Dual Contouring (UDC) as the mesh representation. UDC discretizes a mesh in a regular grid and divides it into the face and vertex parts, recovering both complex structures and fine details. As a result, the one-to-one mapping between UDC and mesh resolves the ambiguity problem. In addition, GenUDC adopts a two-stage, coarse-to-fine generative process for 3D mesh generation. It first generates the face part as a rough shape and then the vertex part to craft a detailed shape. Extensive evaluations demonstrate the superiority of UDC as a mesh representation and the favorable performance of GenUDC in mesh generation. The code and trained models are available at <https://github.com/TrepangCat/GenUDC>.

*Corresponding Author.

Permission to make digital or hard copies of all or part of this work for personal or classroom use is granted without fee provided that copies are not made or distributed for profit or commercial advantage and that copies bear this notice and the full citation on the first page. Copyrights for components of this work owned by others than the author(s) must be honored. Abstracting with credit is permitted. To copy otherwise, or republish, to post on servers or to redistribute to lists, requires prior specific permission and/or a fee. Request permissions from permissions@acm.org.

MM '24, October 28–November 1, 2024, Melbourne, VIC, Australia

© 2024 Copyright held by the owner/author(s). Publication rights licensed to ACM.

ACM ISBN 979-8-4007-0686-8/24/10

<https://doi.org/10.1145/3664647.3681241>

CCS Concepts

• **Computing methodologies** → **Mesh models**; • **Information systems** → *Multimedia content creation*.

Keywords

Mesh, 3D Generation, Diffusion Model, Dual Contouring

ACM Reference Format:

Ruowei Wang, Jiaqi Li, Dan Zeng, Xueqi Ma, Zixiang Xu, Jianwei Zhang, and Qijun Zhao. 2024. GenUDC: High Quality 3D Mesh Generation with Unsigned Dual Contouring Representation. In *Proceedings of the 32nd ACM International Conference on Multimedia (MM '24), October 28-November 1, 2024, Melbourne, VIC, Australia*. ACM, New York, NY, USA, 13 pages. <https://doi.org/10.1145/3664647.3681241>

1 Introduction

Mesh plays an important role in 3D content generation and reconstruction [19, 40, 41, 69], AR/VR [20], robotics [18, 65], and autonomous driving [4, 7, 16] and other 3D tasks [39, 66, 69, 76]. It can flexibly represent various complex geometric shapes. High editability allows meshes to be modified and adjusted easily in computer-aided design (CAD). Additionally, it is effortless for users to convert meshes to other 3D representations, e.g., voxels, point clouds, and neural implicit functions. Besides, the rendering pipelines are designed for meshes, enabling high-quality 3D visualization effects. However, employing deep neural networks on meshes is tricky because the numbers of vertices and faces are constantly changing, and modeling the complex topology structure of faces is also an obstacle. To navigate those challenges, a mesh representation compatible with deep learning and a capable generative framework adapted to this mesh representation are both highly desired.

Most existing approaches focus on intermediate representations, e.g., voxels [58, 71], point clouds [1, 34, 46, 47], neural implicit functions [9, 32, 69, 77, 78] and so on, which are highly compatible with deep learning. However, those methods require a post-processing step [8, 10, 12, 27, 44, 59] to extract meshes, resulting in over-smooth surfaces and lacking detailed geometry. PolyGen [52] first treats vertices and faces as sequences and uses transformer networks [67] to generate vertices and then faces. MeshGPT [64] and PolyDiff [2] follow similar ideas but concentrate on faces. All three approaches cannot produce mesh with intricate geometry since the memory limits the number of faces to no more than 2800. MeshDiffusion [42] chooses to combine a deformable tetrahedral grid with Signed Distance Functions (SDF) to model meshes. However, its data preparation is especially slow (Tab. 6), and the generated meshes are crumpled due to the deformable nature of the grid and the inaccurate 2D image supervision.

To employ deep neural networks on meshes and synthesize meshes of high quality with complex structures, we construct a novel framework dubbed **GenUDC** to combine the Unsigned Dual Contouring representation (UDC) with a two-stage, coarse-to-fine generative process, enabling high-quality mesh generation. As a mesh counterpart, UDC consists of a face part and a vertex part. Accordingly, we decompose the mesh generation into two subtasks: the face part generation and vertex part generation. To address these subtasks, we devise a customized pipeline, which involves generating faces first and then vertices.

Table 1: Taxonomy of mesh generation methods.

Method	Representation	Memory	Maximum Num Of Faces
PolyGen [52]	Face Sequence + Vertex Sequence	High	Less Than 2800
MeshGPT [64]	Triangle Face Sequence	High	Less Than 800
PolyDiff [2]	Triangle Face Soup	High	Less Than 800
MeshDiffusion [42]	Deformable Tetrahedral Grid + SDF	Medium	More Than 32768
Ours (GenUDC)	UDC (Regular Grid)	Medium	More Than 32768

Precisely, to find a proper mesh representation, we expand Dual Contouring [27], which has long been regarded as an isosurface reconstruction method, to generation tasks. Thus, we obtain the UDC representation to model meshes as shown in Fig. 1 (a) and Fig. 2. In UDC, we discretize a mesh in a regular grid. The faces part of UDC is a set of tiny faces represented by boolean values. The vertex part of UDC contains all the actual and potential vertices of those tiny faces. Since the values of the face part and vertex part are arranged in a regular grid, we can conveniently employ deep learning-based generative models to learn the distribution of UDC.

Another pivotal component is the two-stage, coarse-to-fine generative process specially designed for UDC. Because the mesh is discretized in UDC, the face part draws the rough shape, and the vertex part describes the details. Consequently, we first employ a latent diffusion model to generate the face part, determining the mesh's rough shape and topological structure. Then, conditioning the rough shape, we take a vertex refiner to generate the vertex part. Such a pipeline is a natural solution for mesh generation. Without this pipeline, the edges would be jagged due to the inaccurate vertex part. We will study the necessity of this pipeline in Sec. 4.4.

Finally, using GenUDC, we can produce high-quality meshes with complex structures and realistic details as shown in Fig. 1 (b) and Fig. 3. Comprehensive experiments demonstrate our superiority over existing ones in mesh generation. In data fitting, compared with MeshDiffusion, our method runs at 3274% times their speed and consumes only 13% of their total memory as shown in Tab. 6.

To summarize, the contributions of this paper are:

- We propose a novel framework, **GenUDC**, utilizing UDC as the representation for high-quality mesh generation.
- We design a two-stage, coarse-to-fine generative pipeline to UDC, which generates faces and then vertices, circumventing the jagged edges problem.
- Extensive experiments demonstrate our method's superior performance in mesh generation and data fitting.

2 Related Work

This section outlines some closely related topics to our study: 3D shape generation, isosurface reconstruction, and diffusion models.

2.1 3D Shape Generation

With the advent of deep learning, researchers have been exploring the generation of 3D voxels [33, 58, 68, 71, 73] and point clouds [1, 3, 14, 25, 28, 31, 36, 46, 47, 62, 72, 74] using neural networks. However, voxels suffer from memory limits, and point clouds lack topology of shapes. Until the dawn of neural implicit function [9, 51, 55], the community finds it an excellent shape representation, which

does not require a lot of memories and can be easily transformed into meshes. The neural implicit function is specially designed for advanced deep neural networks and inspires a lot of work [11, 13, 24, 26, 30, 32, 35, 37, 50, 53, 61, 63, 69, 70, 75, 77, 78]. It utilizes SDF values or occupancy values as the intermediate representation of 3D shapes. By using some isosurface reconstruction methods like Marching Cube [12, 44], and Dual Contouring [27], meshes can be reconstructed from those neural implicit functions. However, this also means those implicit function-based methods still require a post-processing step and cannot directly generate meshes.

Moreover, some works are trying to find a proper mesh representation to generate meshes directly. PolyGen [52], MeshGPT [64], and PolyDiff [2] are inspired by natural language processing to process meshes as sequences. By leveraging the power of transformer network [67], they can theoretically produce vertices and faces of any length. In practice, the limited memory constrains the complexity of synthetic mesh structures, making it difficult for them to generate curved surfaces. A similar work [48] has explored to generate wireframes of mesh. In MeshDiffusion [42], a deformable tetrahedral grid and SDF values are utilized to recover meshes. It supposes all mesh vertices are on the edges of the deformable tetrahedral grid. It can use linear interpolation to compute mesh vertices with the coordinates of adjacent grid points and SDF values. After getting the mesh vertices, it produces faces by connecting mesh vertices in the same tetrahedrons. However, the deformable grid brings ambiguity to the fitting mesh. Two different tetrahedral grids with distinct SDF values may recover the same mesh. In addition, to fit a mesh, the deformable grid is trained in the supervision of rendered images, which are inaccurate due to various rendering settings. The ambiguity and 2D supervision tend to result in deficient surfaces shown in Fig. 7. As for data preparation, it takes too much time and memory to fit a tetrahedral grid on a shape due to the 2D supervision, as shown in Tab. 6.

In contrast to sequence-based methods [2, 52, 64], our method is capable of using limited memory to generate a diverse range of mesh structures, such as flat surfaces, thin parts, curved surfaces, sharp parts, and so on, as shown in Fig. 1 (b). Compared with MeshDiffusion [42], we use a regular grid to fit meshes with more accurate results, less processing time, and less memory, as shown in Tab. 6 and Fig. 7. We taxonomize methods that can directly generate meshes in Tab. 1. We present more details of the data fitting comparison between MeshDiffusion and ours in Sec. 4.5.

2.2 Isosurface Reconstruction

Typically, isosurface reconstruction methods extract meshes from volume data (e.g. voxels and SDF volumes). As a pioneering work, the original Marching Cubes (MC) method is proposed by Lorensen and Cline [44]. It discretizes a mesh into a regular grid and creates approximative surfaces in each cube according to intersections between the mesh and grid. Its most well-known variant, MC33 [12], can even model all possible topological cases in a cube. However, since vertices of approximative surfaces are on the edges of the grid, it is hard for the marching cubes method to model sharp parts. The Dual Contouring method (DC) [27] is thus proposed. Its vertices of approximative faces (also called dual faces) are in the cubes. So DC can recover sharp parts. With the rise of deep learning,

Deep Marching Cubes [38] first applied deep learning to isosurface reconstruction. Neural Marching Cubes (NMC) [10] and Neural Dual Contouring (NDC) [8] focus on building a learnable version of MC and DC. Manifold Dual Contouring [59] and FlexiCubes [60] try to solve the non-manifold problem in DC. VoroMesh [49] introduces Voronoi diagrams to isosurface reconstruction.

All isosurface reconstruction methods focus on transforming 3D data of various forms into mesh counterparts. In contrast, we adopt UDC and expand it to shape generation by learning the distribution of the UDC representations. In other sections, with a little abuse of the abbreviation, we refer to UDC representation as UDC.

2.3 Diffusion Models

Diffusion models are a class of deep generative models that play an important role in artificial intelligence generated content (AIGC). It achieves pleasant results in various applications, such as image generation [23, 56], shape generation [42], text-to-3D [13, 35], etc. Diffusion models are designed to model the step-by-step transformations between a simple distribution (e.g. Gaussian distribution) and a complex distribution of data. Once trained, a diffusion model can map a sample of the simple distribution to the desired data distribution. As a milestone of diffusion models, the Denoising Diffusion Probabilistic Model (DDPM) [23] introduces variational inference into diffusion models and shows greater potential over generative adversarial networks [17]. But it still suffers from the huge memory requirement. Therefore, the latent diffusion model (LDM) [56] proposes to train diffusion models in a low-dimensional latent space instead of the high-dimensional data space. It has been demonstrated that this technique can speed up training and reduce memory footprints without degradation of generation quality. In this paper, we adopt the LDM in the face part generation (see Sec. 3.3) since the regular grid takes a lot of memory footprints.

3 Method

3.1 Overview

How to represent meshes and process meshes with neural networks are two critical issues hindering mesh generation. To address them, we propose GenUDC, a novel generative framework for mesh generation. In GenUDC, we discretize a mesh in a regular grid to get its corresponding Unsigned Dual Contouring representation (UDC). Thus, due to UDC's regular grid structure, neural networks can easily be used on both watertight and non-watertight meshes. We further propose a two-stage, coarse-to-fine pipeline adapted to UDC, which generates faces and vertices successively. In summary, we offer a new and straightforward solution for mesh generation.

In the following sections, we first elaborate on UDC in Sec. 3.2. Then, we illustrate our generative models for face generation in Sec. 3.3 and vertex generation in Sec. 3.4. Finally, the implementation details are presented in Sec. 3.5.

3.2 Unsigned Dual Contouring Representation

We have briefly shown the main ideas of the Unsigned Dual Contouring representation (UDC) in Fig. 1 (a) and Fig. 2. For more details, in a grid \mathcal{G} with the size of $(X + 1, Y + 1, Z + 1)$, UDC can

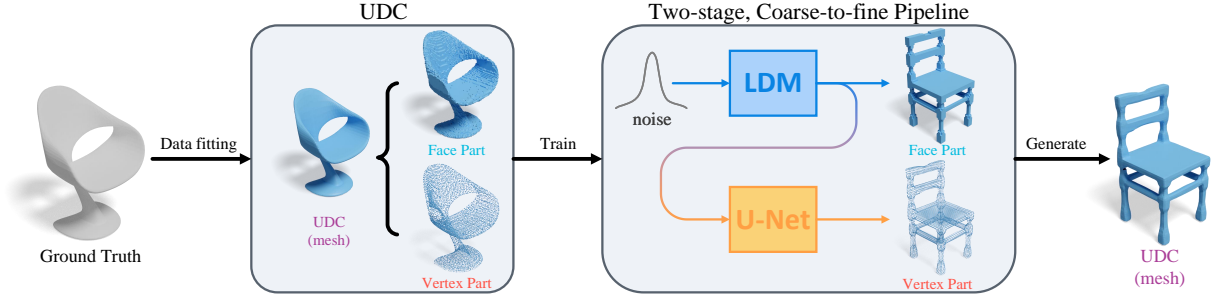


Figure 2: The overview of GenUDC. It consists of UDC and a two-stage, coarse-to-fine generative pipeline. We first translate the meshes to UDCs by data fitting. Then, we take UDCs to train the generative models. After training, we can generate the face part and vertex part to compose the output UDC.

be formalized as:

$$\text{UDC} = \begin{cases} \mathcal{V} \in \mathbb{R}^{3 \times |\mathcal{C}|}, & \text{(vertex part)} \\ \mathcal{F} \in \mathbb{B}^{|\mathcal{E}|}, & \text{(face part)} \end{cases} \quad (1)$$

where \mathcal{C} are the cubes in the grid, \mathcal{V} are the vertices, \mathcal{E} are the edges inside the grid, and \mathcal{F} are the faces (also called dual faces) denoted by the intersection flags of edges. The grid \mathcal{G} contains $(X+1)(Y+1)(Z+1)$ nodes. There are $|\mathcal{C}| = XYZ$ cubes in the grid, and each cube contains a vertex $v \in \mathcal{V}$. Considering the edges along the x-axis, y-axis, and z-axis, there are $|\mathcal{E}| = X(Y-1)(Z-1) + (X-1)Y(Z-1) + (X-1)(Y-1)Z$ inside edges. If the intersection flag of an edge is true, four adjacent vertices make up two triangle faces that are *dual* to the edge. In other words, the edge intersects with one of the two triangle faces when the flag is true. If not, there is no face intersecting with this edge. When translating a UDC to a correlative mesh, we craft faces by traversing all intersection flags in \mathcal{F} and remove a subset of \mathcal{V} which are not in these faces. By this means, faces and remaining vertices comprise the final mesh.

Compared with the traditional SDF-based methods [42, 77], which usually generate over-smooth shapes, UDC can easily model the sharp parts as shown in Fig. 7. In addition, the rigid grid used in UDC is suited for deep neural networks and can produce more realistic surfaces than the deformable grid of MeshDiffusion [42], which will be evaluated in Sec. 4.5. Moreover, UDC has the potential to model non-watertight shapes shown in Fig. 7.

In practice, \mathcal{V} are the relative coordinates in each cube, which means $0 \leq \min(\mathcal{V})$ and $\max(\mathcal{V}) \leq 1$ and \mathcal{F} are boolean values. When $X = Y = Z$, we pad \mathcal{F} with zeros to the same size as \mathcal{V} . We call \mathcal{V} as the vertex part and \mathcal{F} as the face part.

Data Fitting. We follow a similar procedure of DC [27] to fit a mesh with UDC. Given a mesh $\mathcal{M} = (\mathcal{V}^{\mathcal{M}}, \mathcal{F}^{\mathcal{M}})$ and a grid $\mathcal{G} = (\mathcal{C}, \mathcal{E})$, we first find the crossing vertices $\mathcal{V}^{\mathcal{E}}$ of the mesh \mathcal{M} on the edges \mathcal{E} . Then, we compute the normals $\mathcal{N}^{\mathcal{E}}$ of \mathcal{M} at those crossing vertices. With $\mathcal{V}^{\mathcal{E}}$ and $\mathcal{N}^{\mathcal{E}}$, we can create UDC as:

$$\mathcal{V} = f_{\mathcal{V}}(\mathcal{V}^{\mathcal{E}}, \mathcal{N}^{\mathcal{E}}), \quad (2)$$

$$\mathcal{F} = f_{\mathcal{F}}(\mathcal{V}^{\mathcal{E}}, \mathcal{E}). \quad (3)$$

The dual contouring vertices \mathcal{V} should be on the surfaces of \mathcal{M} . So we extrapolate neighboring normals $\mathcal{N}^{\mathcal{E}}$ to find a point of best

fit in each cube:

$$f_{\mathcal{V}} : \{v_{xyz} | \arg \min_{v_{xyz}} \sum_{e \in \mathcal{C}_{xyz}} (\mathcal{N}_e^{\mathcal{E}} \cdot (v_{xyz} - \mathcal{V}_e^{\mathcal{E}}))^2\}, \quad (4)$$

where v_{xyz} is the vertex inside the cube \mathcal{C}_{xyz} which is indexed by (x, y, z) , and e are 12 edges of \mathcal{C}_{xyz} . $0 \leq x < X$, $0 \leq y < Y$, and $0 \leq z < Z$. By default, if there is no $\mathcal{V}_e^{\mathcal{E}}$ or $\mathcal{N}_e^{\mathcal{E}}$ in a cube, v_{xyz} is set to $[0.5, 0.5, 0.5]$.

Besides, we only craft faces \mathcal{F} when \mathcal{M} intersects with an edge $e \in \mathcal{E}$ at the crossing vertex $v \in \mathcal{V}^{\mathcal{E}}$:

$$f_{\mathcal{F}} : \begin{cases} 1, & \text{if } \forall e \in \mathcal{E}, \exists v \in \mathcal{V}^{\mathcal{E}} \text{ is on the } e, \\ 0, & \text{otherwise.} \end{cases} \quad (5)$$

3.3 Face Part Generation

In UDC, we have devised a simple and intuitive method for generating faces by connecting them with intersection flags. If an edge's intersection flag is true, it crosses faces. If not, there is no face. By this means, we can denote all faces of the mesh as boolean values and arrange them into a regular grid as a face tensor $\mathcal{F} \in \mathbb{B}^{|\mathcal{E}|}$. Thus, we can easily employ neural networks to face part generation.

To reduce the memory footprint, we use an LDM [56] to learn the distribution of \mathcal{F} . Our LDM consists of a Variational AutoEncoder (VAE) [29] and a diffusion model [23, 56]. VAE compresses a \mathcal{F} to a latent representation z . Then, we take latent representations z to train our diffusion model. Thus, by extracting the compression process from the generative learning phase, we can speed up the diffusion model training process and reduce the memory footprints. And since the latent space is perceptually equivalent to the input space, there is no quality reduction for the diffusion model. We provide detailed descriptions of VAE and the diffusion model below.

VAE. A VAE comprises an encoder E and a decoder D . Given $\mathcal{F} \in \mathbb{B}^{|\mathcal{E}|}$, we first normalize \mathcal{F} to $[-1.0, 1.0]$ using min-max normalization. Then E encodes \mathcal{F} to a mean code $\mu \in \mathbb{R}^{c \times d \times h \times w}$ and a standard deviation code $\sigma \in \mathbb{R}^{c \times d \times h \times w}$. We use the mean code μ as the latent code $z \in \mathbb{R}^{c \times d \times h \times w}$ without reparameterization, which differs from the typical VAE. Finally, D decodes z back to the face tensor $\mathcal{F}_{pred} = D(z)$. We train our VAE with the mean squared error (MSE) loss and the Kullback-Leibler divergence (KL) loss:

$$\mathcal{L}_{vae} = \mathcal{L}_{mse}(D(E(\mathcal{F})), \mathcal{F}) + KL(\mathcal{N}(\mu, \sigma) || \mathcal{N}(0, 1)). \quad (6)$$

Since we do not use the reparameterization technique, our VAE is more like an autoencoder (AE) producing compact latent codes (close to zero).

Diffusion Model. After encoding the face part \mathcal{F} to the latent code z with our VAE, we employ a diffusion model [23, 56] to the latent code distribution $p(z)$. We first normalize $z_0 \in p(z)$ to $[-1.0, 1.0]$. Then, through a series of diffusion steps, we introduce the controlled Gaussian noise ϵ to z_0 and transform it to $z_t = \sqrt{\bar{\alpha}_t}z_0 + \sqrt{1 - \bar{\alpha}_t}\epsilon$, where $t = 1 \dots T$ and $\bar{\alpha}_t = \prod_{i=1}^t \alpha_i$, $\alpha_t = 1 - \beta_t$ and β_t is the predefined variance. The diffusion model θ is trained to predict the noise ϵ , aiming at reversing the diffusion steps. The training objective is

$$\mathcal{L}_{dm} = \mathbb{E}_{x,t,\epsilon \sim \mathcal{N}(0,1)} \|\epsilon - \epsilon_\theta(z_t, t)\|_1. \quad (7)$$

After training, to generate a face part \mathcal{F} , a sampled Gaussian noise $\epsilon \sim \mathcal{N}(0, 1)$ is seen as z_T . Then, our trained diffusion model denoises z_T to z_0 . z_0 is further denormalized from $[-1.0, 1.0]$ to the original data range of $p(z)$. Finally, the D decodes denormalized z_0 to \mathcal{F} .

More details of the network are in the supplemental material.

3.4 Vertex Part Generation

The vertex part \mathcal{V} is a set of relative vertex coordinates, and all vertices are arranged in a regular grid. Each vertex is in a cube of this grid. The vertex part contains all actual and potential vertices of a mesh. Since several vertices compose a face, there is a tight correlation between \mathcal{V} and \mathcal{F} . Therefore, learning this correlation is a crucial problem in the vertex part generation.

In UDC, when the face part is determined, the rough shape is known, and the variance of the vertex part is limited. So we treat the vertex part generation as a regression task. We take a vertex refiner to generate \mathcal{V} conditioned on \mathcal{F} . Here, we use a 3D version of U-Net [57] as the vertex refiner. Note that \mathcal{F} is padded to the same size as \mathcal{V} described in Sec. 3.2. Firstly, we normalize the face part \mathcal{F} and the vertex part \mathcal{V} to $[-1.0, 1.0]$. Secondly, the vertex refiner takes the \mathcal{F} as the conditional input and generates a vertex part $\mathcal{V}_{pred} \in \mathbb{R}^{3 \times |C|}$ as shown in Fig. 2. We compare \mathcal{V}_{pred} with the ground truth \mathcal{V}_{gt} to train networks:

$$\mathcal{L}_{float} = \mathcal{L}_{mse}(\mathcal{V}_{gt}, \mathcal{V}_{pred}), \quad (8)$$

$$\mathcal{V}_{pred} = \text{Unet3D}(\mathcal{F}), \quad (9)$$

where \mathcal{L}_{mse} is MSE loss. \mathcal{V}_{gt} is the ground truth vertices paired with \mathcal{F} . In the inference phase, \mathcal{V}_{pred} is denormalized from $[-1.0, 1.0]$ to $[0.0, 1.0]$.

This is a natural and efficient solution to learn the correlation between \mathcal{F} and \mathcal{V} for vertex part generation with reasonable training costs. If we eliminate the vertex refiner and generate \mathcal{F} and \mathcal{V} together, synthesized meshes will contain jagged edges due to inaccurate vertex coordinates as discussed in Sec. 4.4.

More details of the network are in the supplemental material.

3.5 Implementation Details

If not specified otherwise, we set $X = Y = Z = 64$ for the grid \mathcal{G} and $c = 64$, $d = h = w = 16$ for the latent code z . During training, \mathcal{V} and \mathcal{F} are normalized to $[-1.0, 1.0]$. At the final step of mesh generation, we denormalize the generated \mathcal{V} and \mathcal{F} to $[0.0, 1.0]$ and keep \mathcal{V} as floating-point numbers and \mathcal{F} as boolean values. We train the VAE

and U-Net with all five categories as told in Sec. 4.1. In contrast, the diffusion model is trained in a category-specific manner. We use the AdamW optimizer [45] with $\beta_1, \beta_2 = [0.9, 0.999]$ for all networks. Empirically, large β values can make our diffusion model produce realistic meshes. During the inference of diffusion models, we adopt the sampling method in Denoising Diffusion Probabilistic Models [23] and set the inference step as 1000.

4 Experiments

4.1 Data

Following the protocol of MeshDiffusion [42], we use the ShapeNet Core (v1) dataset [5] to train and test our networks. Airplane, car, chair, refile, and table — five categories are used in our experiments. For each category, we split all data like [21] and [77] do: 70% as the training set, 20% as the test set, 10% as the validation set. To be clear, the validation set is not used. For a fair comparison, we remove the interior of shapes. We apply the data-fitting method in Sec. 3.2 to generate UDC for all mesh data.

4.2 Shape Generation

To evaluate the quality of shape generation, we compare our method with IM-GAN [9], SDF-StyleGAN [77], MeshDiffusion [42] and, LAS-Diffusion [78]. IM-GAN, SDF-StyleGAN, and LAS-Diffusion are neural implicit function-based shape generation methods. IM-GAN predicts the occupancy values. Similarly, SDF-StyleGAN and LAS-Diffusion predict the SDFs. We apply MC to create meshes from synthesized implicit representations, following their protocols. MeshDiffusion is a mesh generation method that uses a deformable tetrahedral grid and SDF values to generate meshes directly. We do not compare ours with PolyGen, MeshGPT, and PolyDiff because it is unfair that their faces are limited to no more than 2800, and they cannot produce complex geometric shapes.

Four metrics and three kinds of distances are used in the quantitative experiments (Tab. 2). We take the test dataset as the reference set \mathcal{B} and generate samples \mathcal{A} of the same number, i.e. $|\mathcal{A}| = |\mathcal{B}|$. To calculate chamfer distance (COV) and earth mover's distance (EMD), we sample 2048 points for each mesh of \mathcal{A} and \mathcal{B} . Note that all point clouds are normalized to $[-1.0, 1.0]$, and meshes are normalized to $[-0.5, 0.5]$. The supplementary materials elaborate on more details of metrics.

Quantitative evaluation. We present metric values in Tab. 2. Our method outperforms others in most cases, indicating that our approach is superior in quality, diversity, and distribution. Particularly in the car and airplane category, our method performs significantly better than others. It can be attributed to our excellent ability to generate details, considering the minimal intra-class variation within cars. We also achieve good performance in high resolution, shown in Tab. 3.

Qualitative evaluation. We show rendered meshes of various methods in Fig. 3. As seen, neural implicit function-based methods tend to produce over-smooth shapes and inaccurate parts, e.g., arms of chairs, wheels of cars, and legs of tables. MeshDiffusion usually produces pits on surfaces due to the ambiguity and inaccurate 2D supervision, which we have examined the reason in Sec. 2.1. The Laplacian smoothing used in MeshDiffusion reduces its generation

Table 2: Quantitative evaluation of shape generation in 64^3 resolution.

	Method	MMD (\downarrow)			COV ($\%, \uparrow$)			1-NNA ($\%, \downarrow$)			JSD ($10^{-3}, \downarrow$)
		CD $\times 10^3$	EMD $\times 10$	LFD	CD	EMD	LFD	CD	EMD	LFD	
Chair	IM-GAN	13.928	1.816	3615	49.64	41.96	47.79	58.59	69.05	68.58	6.298
	SDF-StyleGAN	15.763	1.839	3730	45.60	45.50	43.95	63.25	67.80	67.66	6.846
	MeshDiffusion	13.212	1.731	3472	46.00	46.71	42.11	53.69	57.63	63.02	5.038
	Ours	14.083	1.653	2924	48.08	48.60	47.94	59.18	58.67	60.84	4.837
Car	IM-GAN	5.209	1.197	2645	28.26	24.92	30.73	95.69	94.79	89.30	42.586
	SDF-StyleGAN	5.064	1.152	2623	29.93	32.06	41.93	88.34	88.31	84.13	15.960
	MeshDiffusion	4.972	1.196	2477	34.07	25.85	37.53	81.43	87.84	70.83	12.384
	Ours	3.753	0.854	1191	45.67	46.53	45.73	60.80	58.33	62.23	2.839
Airplane	IM-GAN	3.736	1.110	4939	44.25	37.08	45.86	79.48	82.94	79.11	21.151
	SDF-StyleGAN	4.558	1.180	5326	40.67	32.63	38.20	85.48	87.08	84.73	26.304
	MeshDiffusion	3.612	1.042	4538	47.34	42.15	45.36	66.44	76.26	67.24	11.366
	Ours	3.960	0.902	3167	48.33	50.06	44.13	60.75	56.74	69.16	7.020
Rifle	IM-GAN	3.550	1.058	6240	46.53	37.89	42.32	70.00	72.74	69.26	25.704
	SDF-StyleGAN	4.100	1.069	6475	46.53	40.21	41.47	73.68	73.16	76.84	33.624
	MeshDiffusion	3.124	1.018	5951	52.63	42.11	48.84	57.68	67.79	55.58	19.353
	Ours	3.530	0.849	3493	48.42	51.58	50.53	56.63	55.05	55.58	10.951
Table	IM-GAN	11.378	1.567	3400	51.04	49.20	51.04	65.96	63.17	62.49	4.865
	SDF-StyleGAN	13.896	1.615	3423	42.21	41.80	42.98	68.35	68.21	66.19	4.603
	MeshDiffusion	11.405	1.548	3427	49.56	50.33	51.92	59.35	59.47	58.97	4.310
	Ours	11.998	1.564	2683	46.36	50.41	47.12	61.46	59.43	60.75	3.822

Table 3: Quantitative evaluation of shape generation in 128^3 resolution on airplane category.

Method	MMD (\downarrow)			COV ($\%, \uparrow$)			1-NNA ($\%, \downarrow$)			JSD ($10^{-3}, \downarrow$)
	CD $\times 10^3$	EMD $\times 10$	LFD	CD	EMD	LFD	CD	EMD	LFD	
LAS-Diffusion	4.654	0.56	3142	37.45	35.72	42.15	79.48	84.67	71.51	33.137
Ours	4.000	0.509	3077	46.72	43.88	42.27	60.01	61.06	69.22	6.873

quality by removing details and thin parts, such as chair arms and legs, rifle barrels, aero engines, and airplane propellers. In contrast, our GenUDC can generate high-quality meshes with realistic appearances, various structures, and rich details. We provide more visual samples in the supplementary materials.

4.3 Comparison with NDC

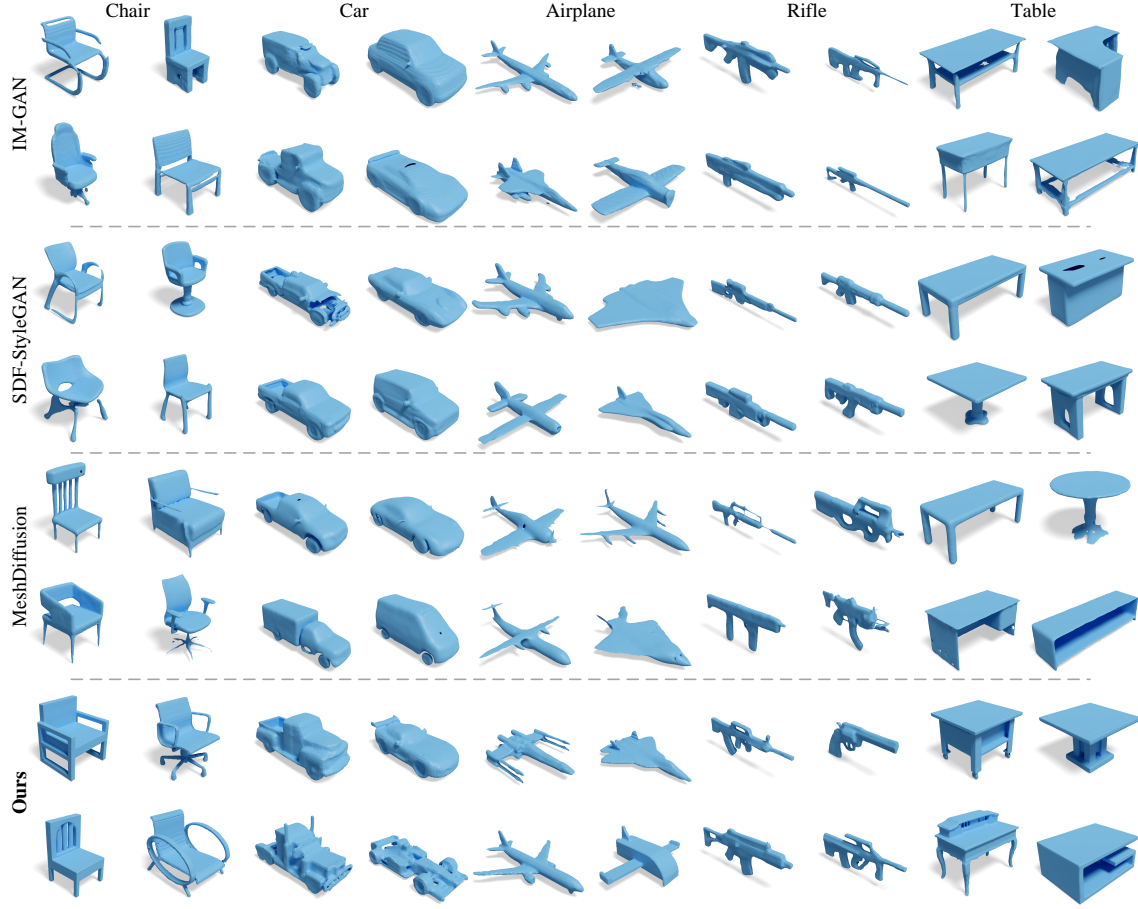
Since NDC [8] is an isosurface reconstruction method, we cannot directly compare GenUDC with NDC. Thus, we train NDC and UNDC networks with the default setting of their codes and the data from the airplane category of ShapeNetCore (v1) [5] for 2500 epochs. After training, we apply them to SDFs to create meshes for comparison. Qualitative evaluations are shown in Tab. 4. The performance of NDC and UNDC is poor due to the distribution gap between SDFs generated by SDF-StyleGAN and SDFs for training NDC, shown in Fig. 4. Fig. 5 shows that NDC and UNDC cannot handle the generated SDFs, resulting in surface distortion and floating artifacts. Overall, integrating NDC (UNDC) into the SDF generation method introduces too many uncertainties, making it unsuitable for mesh generation. In contrast, our GenUDC directly generates high-quality meshes using UDC, demonstrating that our paradigm is more suitable for mesh generation.

4.4 Ablation Study of the Vertex Part Generation

In this section, we compare the GenUDC to the one without the U-Net to demonstrate the necessity of the vertex refiner, i.e., U-Net. In the one without the U-Net, we concatenate the face part \mathcal{F} and vertex part \mathcal{V} as a mesh tensor and then use the LDM to learn the distribution of mesh tensors. Other settings are consistent with the vanilla GenUDC. More network details are in the supplementary materials. Then, we take mesh tensors to train the LDM, learning the joint distribution of \mathcal{F} and \mathcal{V} . At the inference, it simultaneously generates \mathcal{F} and \mathcal{V} . However, it is quite difficult for a single LDM to learn this joint distribution and build the correlation between \mathcal{F} and \mathcal{V} . To prove this, we present some similar samples produced by GenUDC with and without U-Net in Fig. 6. As we can see, removing U-Net results in jagged edges and unsmooth surfaces. Only by modeling the vertex part generation conditioned on the face part, we can learn the correlation between \mathcal{F} and \mathcal{V} . The quantitative evaluation in Tab. 5 also proves our opinion.

4.5 Data Fitting Comparison

Our UDC is a discretized mesh counterpart, which requires a data fitting process. In this section, we demonstrate the superiority of UDC in the data fitting process compared with MeshDiffusion, which uses a deformable tetrahedral grid to discretize a mesh.

Figure 3: Qualitative evaluation of shape generation in 64^3 resolution.Table 4: Quantitative comparison between MC, NDC, UNDC, and ours in 64^3 resolution on the airplane category. We apply those three methods to the same SDFs generated by SDF-StyleGAN. A post-processing step described in [8] is used after UNDC.

Method	MMD (\downarrow)			COV ($\%, \uparrow$)			1-NNA ($\%, \downarrow$)			JSD ($10^{-3}, \downarrow$)
	CD $\times 10^3$	EMD $\times 10$	LFD	CD	EMD	LFD	CD	EMD	LFD	
SDF-StyleGAN + MC	4.459	1.113	3731	41.29	43.88	41.14	81.33	76.89	80.04	20.581
SDF-StyleGAN + NDC	7.341	1.257	3748	17.55	20.64	44.00	94.13	95.30	78.06	133.827
SDF-StyleGAN + UNDC	7.758	1.563	3902	15.57	14.46	41.90	95.24	97.71	80.66	173.030
Ours	3.960	0.902	3167	48.33	50.06	44.13	60.75	56.74	69.16	7.020

Table 5: Quantitative evaluation of ablation study. We compare two methods on the car category following the setting in Sec. 4.2.

Method	MMD (\downarrow)			COV ($\%, \uparrow$)			1-NNA ($\%, \downarrow$)			JSD ($10^{-3}, \downarrow$)
	CD $\times 10^3$	EMD $\times 10$	LFD	CD	EMD	LFD	CD	EMD	LFD	
Ours w/o U-net	15.463	1.702	3073	36.28	42.77	36.06	74.93	72.23	75.18	6.574
Ours w/ U-net	14.083	1.653	2924	48.08	48.60	47.94	59.18	58.67	60.84	4.837

For quantitative evaluation, we randomly select one hundred meshes and record the average processing time and memory footprints in Tab. 6. As shown, UDC outperforms MeshDiffusion in

both speed and memory footprint. The reason is that MeshDiffusion uses the rendered 2D images as the supervision of data fitting. Rendering 2D images requires a lot of GPU and CPU resources, and it takes a long time to fit data. In contrast, we only use the CPU

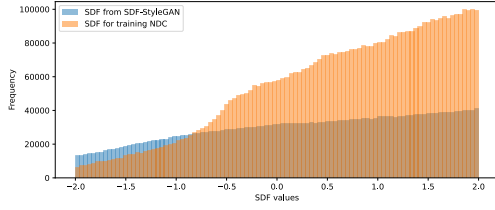


Figure 4: The histogram of SDFs generated by SDF-StyleGAN and SDFs for training NDC. We select 809 SDF grids and only consider SDFs near the surfaces to draw this histogram.

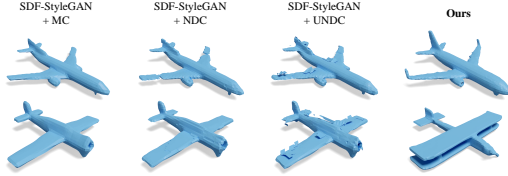


Figure 5: Visual samples of three post-processing methods and ours. We apply those post-processing methods on the same SDFs generated by SDF-StyleGAN.

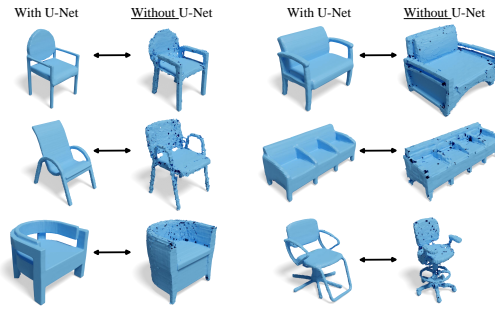


Figure 6: GenUDC with U-Net vs. GenUDC without U-Net. A pair of samples are not the same object but are similar in appearance and structure.

Table 6: Quantitative evaluation of data fitting in terms of mean processing time, GPU memory footprints, and CPU memory footprints of one hundred samples. All the programs are executed in a single thread, using an NVIDIA RTX 3090 GPU, an Intel i7-10700 CPU, and 64GB of memory.

	Processing time (Sec.)	GPU memory (MB)	CPU memory (MB)
MeshDiffusion	1,408	8544	1497
Ours (UDC)	43	0	1266

to directly calculate the fitting vertices and faces of UDC as we elaborate in Sec. 3.2, which is resource-efficient and fast.

To visually illustrate UDC's superiority, we present some samples in Fig. 7. As seen, MeshDiffusion is unavoidable to produce pits on the mesh surfaces and lack of details, such as the line and crack on the car. The reason is the ambiguity and inaccurate 2D

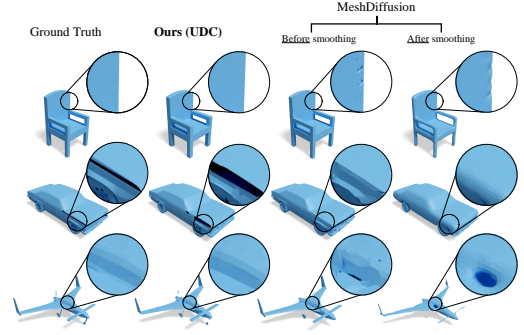


Figure 7: Qualitative evaluation of data fitting. The resolution of those meshes is 64^3 except for the ground truth. In addition, since MeshDiffusion applies a post-processing method to the uneven surfaces of its fitting mesh, we present both raw and smoothed meshes.

supervision discussed in Sec. 2.1. Laplacian smoothing used by MeshDiffusion even removes details and sharp parts instead of the pits. In comparison, UDC can fit flat surfaces, sharp parts, and curved surfaces with details.

5 Limitation

Firstly, our main limitation is the non-manifold issue. Since we adopt UDC as the mesh representation, our method inherits the non-manifold issue from DC. However, such an issue rarely occurs. It can be resolved by "tunneling" through vertices/edges or dividing them with the approaches introduced by [54, 59]. Secondly, the memory footprint constrains the resolution of our results. Thirdly, since the face part is a set of boolean values, our models may predict wrong boolean values, resulting in pits on the surface. We can solve this pit problem with the post-processing method in [8].

6 Conclusion & Future Works

In conclusion, we propose a novel 3D generative framework, GenUDC, using the Unsigned Dual Contouring representation (UDC) for high-quality mesh generation. Our method can directly generate high-quality meshes without using isosurface reconstruction methods. Specifically, following the discretization idea, we fit a mesh in a regular grid to get its UDC representation. Since UDC is composed of the face and vertex parts, we use a two-stage, coarse-to-fine pipeline to learn its distribution. Firstly, we use a latent diffusion model to generate the face part. Secondly, we take a U-Net as a vertex refiner to synthesize the vertex part conditioned on the face part. Experiments demonstrate our superiority over baselines in shape generation and data fitting. The ablation study proves the validity of network design. We believe that our method offers a new paradigm for further work in mesh generation.

In the future, we plan to apply GenUDC to various applications, such as text-to-3D, joint generation of texture and shape, single view 3D reconstruction, shape editing, 3D attacks [15], etc.

Acknowledgments

The research was sponsored by the National Natural Science Foundation of China (No. 62176170, 61773270).

References

- [1] Panos Achlioptas, Olga Diamanti, Ioannis Mitliagkas, and Leonidas Guibas. 2018. Learning representations and generative models for 3D point clouds. In *ICML*.
- [2] Antonio Alliegro, Yawar Siddiqui, Tatiana Tommasi, and Matthias Nießner. 2023. PolyDiff: Generating 3D Polygonal Meshes with Diffusion Models. *arXiv preprint arXiv:2312.11417* (2023).
- [3] Mohammad Samiul Arshad and William J. Beksi. 2020. A Progressive Conditional Generative Adversarial Network for Generating Dense and Colored 3D Point Clouds. In *3DV*.
- [4] Aseem Behl, Omid Hosseini Jafari, Siva Karthik Mustikovela, Hassan Abu Alhaija, Carsten Rother, and Andreas Geiger. 2017. Bounding boxes, segmentations and object coordinates: How important is recognition for 3D scene flow estimation in autonomous driving scenarios?. In *ICCV*.
- [5] Angel X. Chang, Thomas Funkhouser, Leonidas Guibas, Pat Hanrahan, Qixing Huang, Zimo Li, Silvio Savarese, Manolis Savva, Shuran Song, Hao Su, Jianxiong Xiao, Li Yi, and Fisher Yu. 2015. *ShapeNet: An Information-Rich 3D Model Repository*. Technical Report arXiv:1512.03012 [cs.GR].
- [6] Ding-Yun Chen, Xiao-Pei Tian, Yu-Te Shen, and Ming Ouhyoung. 2003. On visual similarity based 3D model retrieval. In *CGF*.
- [7] Yiping Chen, Jingkan Wang, Jonathan Li, Cewu Lu, Zhipeng Luo, Han Xue, and Cheng Wang. 2018. LiDAR-Video Driving Dataset: Learning Driving Policies Effectively. In *CVPR*.
- [8] Zhiqin Chen, Andrea Tagliasacchi, Thomas Funkhouser, and Hao Zhang. 2022. Neural dual contouring. *TOG* (2022).
- [9] Zhiqin Chen and Hao Zhang. 2019. Learning Implicit Fields for Generative Shape Modeling. In *CVPR*.
- [10] Zhiqin Chen and Hao Zhang. 2021. Neural Marching Cubes. *TOG* (2021).
- [11] Yen-Chi Cheng, Hsin-Ying Lee, Sergey Tulyakov, Alexander G. Schwing, and Liang-Yan Gui. 2023. SDFusion: Multimodal 3D Shape Completion, Reconstruction, and Generation. In *CVPR*.
- [12] Evgeni Chernyaev. 1995. Marching cubes 33: Construction of topologically correct isosurfaces. *Technical Report CN/95-17*. CERN. (1995).
- [13] Gene Chou, Yuval Bahat, and Felix Heide. 2023. Diffusion-SDF: Conditional Generative Modeling of Signed Distance Functions. In *ICCV*.
- [14] Rinon Gal, Amit Bermano, Hao Zhang, and Daniel Cohen-Or. 2021. MRGAN: Multi-Rooted 3D Shape Representation Learning With Unsupervised Part Disentanglement. In *ICCV*.
- [15] Kuofeng Gao, Jiawang Bai, Baoyuan Wu, Mengxi Ya, and Shu-Tao Xia. 2023. Imperceptible and robust backdoor attack in 3d point cloud. *TIFS* (2023).
- [16] Andreas Geiger, Philip Lenz, and Raquel Urtasun. 2012. Are we ready for autonomous driving? The KITTI vision benchmark suite. In *CVPR*.
- [17] Ian Goodfellow, Jean Pouget-Abadie, Mehdi Mirza, Bing Xu, David Warde-Farley, Sherjil Ozair, Aaron Courville, and Yoshua Bengio. 2014. Generative adversarial nets. In *NeurIPS*.
- [18] Joris Guerry, Alexandre Boulch, Bertrand Le Saux, Julien Moras, Aurélien Plyer, and David Filliat. 2017. Snapnet-r: Consistent 3D multi-view semantic labeling for robotics. In *ICCVW*.
- [19] Benoit Guillard, Edoardo Remelli, Pierre Yvernay, and Pascal Fua. 2021. Sketch2Mesh: Reconstructing and Editing 3D Shapes from Sketches. In *ICCV*.
- [20] Lei Han, Tian Zheng, Yinheng Zhu, Lan Xu, and Lu Fang. 2020. Live semantic 3D perception for immersive augmented reality. *TVCG* (2020).
- [21] Christian Häne, Shubham Tulsiani, and Jitendra Malik. 2017. Hierarchical surface prediction for 3D object reconstruction. In *3DV*.
- [22] Kaiming He, Xiangyu Zhang, Shaoqing Ren, and Jian Sun. 2016. Deep Residual Learning for Image Recognition. In *CVPR*.
- [23] Jonathan Ho, Ajay Jain, and Pieter Abbeel. 2020. Denoising diffusion probabilistic models. *NeurIPS*.
- [24] Ka-Hei Hui, Ruihui Li, Jingyu Hu, and Chi-Wing Fu. 2022. Neural wavelet-domain diffusion for 3D shape generation. In *SIGGRAPH Asia*.
- [25] Le Hui, Rui Xu, Jin Xie, Jianjun Qian, and Jian Yang. 2020. Progressive point cloud deconvolution generation network. In *ECCV*.
- [26] Moritz Ibing, Isaak Lim, and Leif Kobbelt. 2021. 3D Shape Generation With Grid-Based Implicit Functions. In *CVPR*.
- [27] Tao Ju, Frank Losasso, Scott Schaefer, and Joe Warren. 2002. Dual Contouring of Hermite Data. In *TOG*.
- [28] Hyeonju Kim, Hyeonseung Lee, Woo Hyun Kang, Joun Yeop Lee, and Nam Soo Kim. 2020. Softflow: Probabilistic framework for normalizing flow on manifolds. In *NeurIPS*.
- [29] Diederik P Kingma and Max Welling. 2014. Auto-Encoding Variational Bayes. In *ICLR*.
- [30] Marian Kleineberg, Matthias Fey, and Frank Weichert. 2020. Adversarial Generation of Continuous Implicit Shape Representations. In *EG*.
- [31] Roman Klokov, Edmond Boyer, and Jakob Verbeek. 2020. Discrete point flow networks for efficient point cloud generation. In *ECCV*.
- [32] Juil Koo, Seungwoo Yoo, Minh Hieu Nguyen, and Minhyuk Sung. 2023. SALAD: Part-Level Latent Diffusion for 3D Shape Generation and Manipulation. In *ICCV*.
- [33] Jun Li, Chengjie Niu, and Kai Xu. 2020. Learning part generation and assembly for structure-aware shape synthesis. In *AAAI*.
- [34] Jiaxin Li, Feiyu Zhu, Xiao Yang, and Qijun Zhao. 2021. 3D face point cloud super-resolution network. In *IJCB*.
- [35] Muheng Li, Yueqi Duan, Jie Zhou, and Jiwen Lu. 2023. Diffusion-SDF: Text-To-Shape via Voxelized Diffusion. In *CVPR*.
- [36] Ruihui Li, Xianzhi Li, Ka-Hei Hui, and Chi-Wing Fu. 2021. SP-GAN: Sphere-guided 3D shape generation and manipulation. *TOG* (2021).
- [37] Yuhua Li, Yishun Dou, Xuanhong Chen, Bingbing Ni, Yilin Sun, Yutian Liu, and Fuzhen Wang. 2023. Generalized Deep 3D Shape Prior via Part-Discretized Diffusion Process. In *CVPR*.
- [38] Yiyi Liao, Simon Donné, and Andreas Geiger. 2018. Deep Marching Cubes: Learning Explicit Surface Representations. In *CVPR*.
- [39] Feng Liu, Jun Hu, Jianwei Sun, Yang Wang, and Qijun Zhao. 2017. Multi-dim: A multi-dimensional face database towards the application of 3D technology in real-world scenarios. In *IJCB*.
- [40] Feng Liu and Xiaoming Liu. 2022. 2D GANs Meet Unsupervised Single-View 3D Reconstruction. In *ECCV*.
- [41] Feng Liu, Luan Tran, and Xiaoming Liu. 2021. Fully Understanding Generic Objects: Modeling, Segmentation, and Reconstruction. In *CVPR*.
- [42] Zhen Liu, Yao Feng, Michael J Black, Derek Nowrouzezahrai, Liam Paull, and Weiyang Liu. 2023. Meshdiffusion: Score-based generative 3D mesh modeling. *ICLR*.
- [43] David Lopez-Paz and Maxime Oquab. 2017. Revisiting classifier two-sample tests. In *ICLR*.
- [44] William E Lorensen and Harvey E Cline. 1987. Marching cubes: A high resolution 3D surface construction algorithm. In *SIGGRAPH*.
- [45] Ilya Loshchilov and Frank Hutter. 2017. Decoupled weight decay regularization. *arXiv preprint arXiv:1711.05101* (2017).
- [46] Shitong Luo and Wei Hu. 2021. Diffusion probabilistic models for 3D point cloud generation. In *CVPR*.
- [47] Zhaoyang Lyu, Jinyi Wang, Yuwei An, Ya Zhang, Dahua Lin, and Bo Dai. 2023. Controllable Mesh Generation Through Sparse Latent Point Diffusion Models. In *CVPR*.
- [48] Xueqi Ma, Yilin Liu, Wenjun Zhou, Ruowei Wang, and Huia Huang. 2024. Generating 3D House Wireframes with Semantics. In *ECCV*.
- [49] Nissim Maruani, Roman Klokov, Maks Ovsjanikov, Pierre Alliez, and Mathieu Desbrun. 2023. VoroMesh: Learning Watertight Surface Meshes with Voronoi Diagrams. In *ICCV*.
- [50] Tejaswini Medi, Jawad Tayyub, Muhammad Sarmad, Frank Lindseth, and Margret Keuper. 2023. FullFormer: Generating Shapes Inside Shapes. *arXiv preprint arXiv:2303.11235* (2023).
- [51] Lars Mescheder, Michael Oechsle, Michael Niemeyer, Sebastian Nowozin, and Andreas Geiger. 2019. Occupancy Networks: Learning 3D Reconstruction in Function Space. In *CVPR*.
- [52] Charlie Nash, Yaroslav Ganin, SM Ali Eslami, and Peter Battaglia. 2020. Polygen: An autoregressive generative model of 3D meshes. In *ICML*.
- [53] Weizhi Nie, Ruidong Chen, Weijie Wang, Bruno Lepri, and Nicu Sebe. 2023. T2TD: Text-3D Generation Model based on Prior Knowledge Guidance. *arXiv preprint arXiv:2305.15753* (2023).
- [54] Gregory M. Nielson. 2004. Dual marching cubes. In *IEEE VIS*.
- [55] Jeong Joon Park, Peter Florence, Julian Straub, Richard Newcombe, and Steven Lovegrove. 2019. DeepSDF: Learning continuous signed distance functions for shape representation. In *CVPR*.
- [56] Robin Rombach, Andreas Blattmann, Dominik Lorenz, Patrick Esser, and Björn Ommer. 2022. High-Resolution Image Synthesis With Latent Diffusion Models. In *CVPR*.
- [57] Olaf Ronneberger, Philipp Fischer, and Thomas Brox. 2015. U-Net: Convolutional Networks for Biomedical Image Segmentation. In *MICCAI*.
- [58] Aditya Sanghi, Rao Fu, Vivian Liu, Karl D.D. Willis, Hooman Shayani, Amir H. Khasahmadi, Srinath Sridhar, and Daniel Ritchie. 2023. CLIP-Sculptor: Zero-Shot Generation of High-Fidelity and Diverse Shapes From Natural Language. In *CVPR*.
- [59] Scott Schaefer, Tao Ju, and Joe Warren. 2007. Manifold Dual Contouring. *TVCG* (2007).
- [60] Tianchang Shen, Jacob Munkberg, Jon Hasselgren, Kangxue Yin, Zian Wang, Wenzheng Chen, Zan Gojcic, Sanja Fidler, Nicholas Sharp, and Jun Gao. 2023. Flexible isosurface extraction for gradient-based mesh optimization. *TOG* (2023).
- [61] Jaehyeok Shim, Changwoo Kang, and Kyungdon Joo. 2023. Diffusion-Based Signed Distance Fields for 3D Shape Generation. In *CVPR*.
- [62] Dong Wook Shu, Sung Woo Park, and Junseok Kwon. 2019. 3D point cloud generative adversarial network based on tree structured graph convolutions. In

ICCV.

- [63] J. Ryan Shue, Eric Ryan Chan, Ryan Po, Zachary Ankner, Jiajun Wu, and Gordon Wetzstein. 2023. 3D Neural Field Generation Using Triplane Diffusion. In *CVPR*.
- [64] Yawar Siddiqui, Antonio Alliegro, Alexey Artemov, Tatiana Tommasi, Daniele Sirigatti, Vladislav Rosov, Angela Dai, and Matthias Nießner. 2023. Meshgpt: Generating triangle meshes with decoder-only transformers. *arXiv preprint arXiv:2311.15475* (2023).
- [65] Keisuke Tateno, Federico Tombari, Iro Laina, and Nassir Navab. 2017. Cnn-slam: Real-time dense monocular slam with learned depth prediction. In *CVPR*.
- [66] Xiaoguang Tu, Yingtian Zou, Jian Zhao, Wenjie Ai, Jian Dong, Yuan Yao, Zhikang Wang, Guodong Guo, Zhifeng Li, Wei Liu, and Jiashi Feng. 2022. Image-to-Video Generation via 3D Facial Dynamics. *TCSVT* (2022).
- [67] Ashish Vaswani, Noam Shazeer, Niki Parmar, Jakob Uszkoreit, Llion Jones, Aidan N Gomez, Łukasz Kaiser, and Illia Polosukhin. 2017. Attention is All you Need. In *NeurIPS*.
- [68] Hao Wang, Nadav Schor, Ruizhen Hu, Haibin Huang, Daniel Cohen-Or, and Hui Huang. 2018. Global-to-Local Generative Model for 3D Shapes. *TOG* (2018).
- [69] Ruowei Wang, Yu Liu, Pei Su, Jianwei Zhang, and Qijun Zhao. 2023. 3D Semantic Subspace Traverser: Empowering 3D Generative Model with Shape Editing Capability. In *ICCV*.
- [70] Jiacheng Wei, Hao Wang, Jiashi Feng, Guosheng Lin, and Kim-Hui Yap. 2023. TAPS3D: Text-Guided 3D Textured Shape Generation From Pseudo Supervision. In *CVPR*.
- [71] Jiajun Wu, Chengkai Zhang, Tianfan Xue, Bill Freeman, and Josh Tenenbaum. 2016. Learning a probabilistic latent space of object shapes via 3D generative-adversarial modeling. In *NeurIPS*.
- [72] Jianwen Xie, Yifei Xu, Zilong Zheng, Song-Chun Zhu, and Ying Nian Wu. 2021. Generative PointNet: Deep Energy-Based Learning on Unordered Point Sets for 3D Generation, Reconstruction and Classification. In *CVPR*.
- [73] Jianwen Xie, Zilong Zheng, Ruiqi Gao, Wenguan Wang, Song-Chun Zhu, and Ying Nian Wu. 2018. Learning Descriptor Networks for 3D Shape Synthesis and Analysis. In *CVPR*.
- [74] Guandao Yang, Xun Huang, Zekun Hao, Ming-Yu Liu, Serge Belongie, and Bharath Hariharan. 2019. Pointflow: 3D point cloud generation with continuous normalizing flows. In *ICCV*.
- [75] Biao Zhang, Jiapeng Tang, Matthias Nießner, and Peter Wonka. 2023. 3DShape2VecSet: A 3D Shape Representation for Neural Fields and Generative Diffusion Models. *TOG* (2023).
- [76] Tingting Zhang, Qijun Zhao, and Pubu Danzeng. 2021. Bird Keypoint Detection via Exploiting 2D Texture and 3D Geometric Features. In *ICIG*.
- [77] Xinyang Zheng, Yang Liu, Pengshuai Wang, and Xin Tong. 2022. SDF-StyleGAN: Implicit SDF-Based StyleGAN for 3D Shape Generation. In *CGF*.
- [78] Xin-Yang Zheng, Hao Pan, Peng-Shuai Wang, Xin Tong, Yang Liu, and Heung-Yeung Shum. 2023. Locally Attentional SDF Diffusion for Controllable 3D Shape Generation. *SIGGRAPH*.

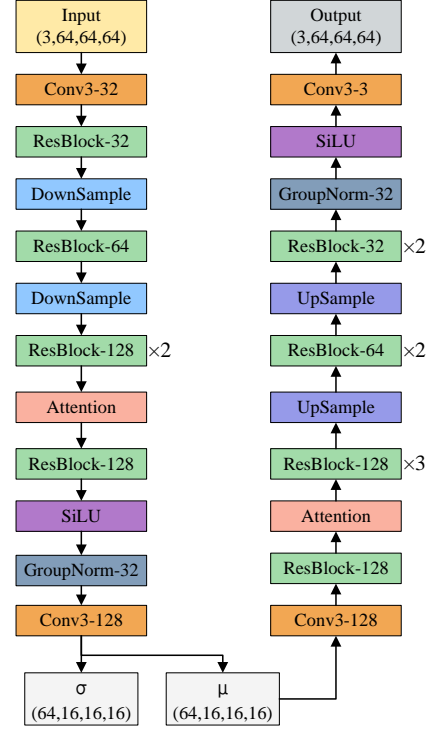


Figure H: Our VAE network for 64 resolution.

A The Architecture of Networks

We show the architecture of our networks in Fig. H, Fig. I, Fig. J, Fig. K, and Fig. L. Specifically, Conv k - x is the convolution layer with k kernel size, x output channels, 1 stride, 1 padding. ResBlock- x is the ResNet block [22] with x output channels. We present the details of ResBlock- x in Fig. M. SiLU is the silu function. GroupNorm- x is the group normalization with x groups. The scale factor of DownSample and UpSample is 2. Attention is the attention block. FC- x is the fully connected layer with x output channels.

B diffusion model

A diffusion model consists of two opposite processes: the forward process and the reverse process. Given the latent representation $z_0 \sim p(z_0)$ as the data, the forward process adds the controlled Gaussian noise ϵ to z_0 for T times:

$$q(z_T|z_0) = \prod_{t=1}^T q(z_t|z_{t-1}), \quad (10)$$

$$q(z_t|z_{t-1}) = N(z_t; \sqrt{\alpha_t}z_{t-1}, \beta_t I), \quad (11)$$

where $\alpha_t = 1 - \beta_t$, and β_t is the predefined variance. In contrast, the reverse process denoises z_T to z_0 :

$$p_\theta(z_0|z_T) = \prod_{t=1}^T p_\theta(z_{t-1}|z_t), \quad (12)$$

$$p_\theta(z_{t-1}|z_t) = N(z_{t-1}; \mu_\theta(z_t, t), \beta_t I). \quad (13)$$

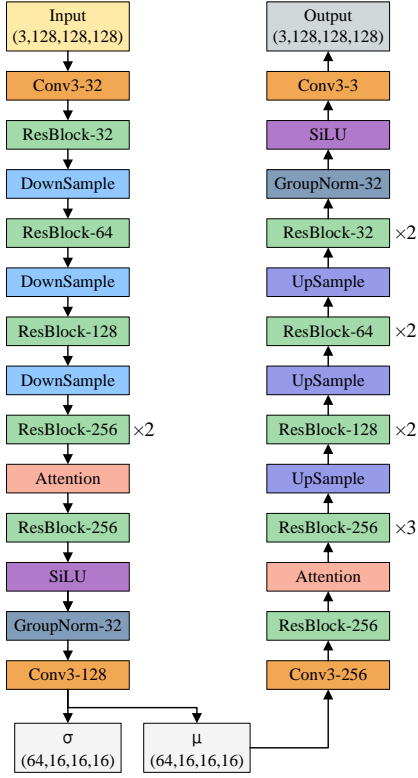


Figure I: Our VAE network for 128 resolution.

According to the method in DDPM [23], we reparameterize $\mu_{\theta}(z_t, t)$ as:

$$\mu_{\theta}(z_t, t) = \frac{1}{\sqrt{\alpha_t}} \left(z_t - \frac{\beta_t}{\sqrt{1 - \alpha_t}} \epsilon_{\theta}(z_t, t) \right), \quad (14)$$

$$z_t = \sqrt{\bar{\alpha}_t} z_0 + \sqrt{1 - \bar{\alpha}_t} \epsilon, \quad \bar{\alpha}_t = \prod_{i=1}^t \alpha_i, \quad (15)$$

where $\epsilon \sim \mathcal{N}(0, 1)$ is the noise. In the cycle of the forward process and the reverse process, the noise $\epsilon_{\theta}(z_t, t)$ is the only unknown value. Thus, we predict $\epsilon_{\theta}(z_t, t)$ by a neural network parameterized as θ to complete the cycle.

We train the network ϵ_{θ} with:

$$\mathcal{L}_{dm} = \mathbb{E}_{z_t, t, \epsilon \sim \mathcal{N}(0, 1)} \|\epsilon - \epsilon_{\theta}(z_t, t)\|_1. \quad (16)$$

In the forward process, we add the noise ϵ to z_0 for getting z_t as shown in Eq. (15), and train the network ϵ_{θ} to fit ϵ . After training, our U-Net denoises $z_T \sim \mathcal{N}(0, 1)$ to z_0 in the reverse process.

C Metrics

Chamfer distance (CD) measures the similarity between two point clouds. The CD is formulated as:

$$CD(A, B) = \sum_{a \in A} \min_{b \in B} \|a - b\|_2^2 + \sum_{b \in B} \min_{a \in A} \|a - b\|_2^2, \quad (17)$$

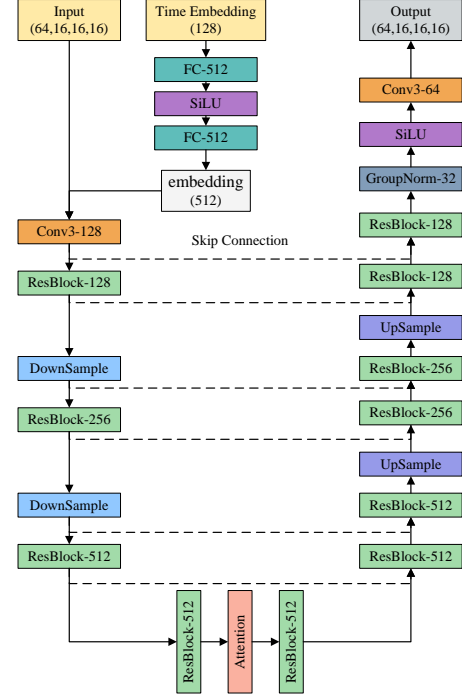


Figure J: Our diffusion model for 64 and 128 resolution.

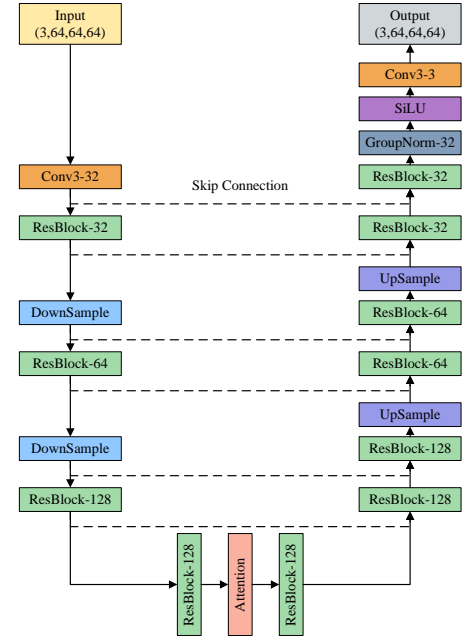


Figure K: Our vertex refiner (U-Net) for 64 resolution.

where A and B are generated point clouds and reference point clouds.

Earth mover's distance (EMD) is a metric of dissimilarity between two distributions and can be also used to measure the

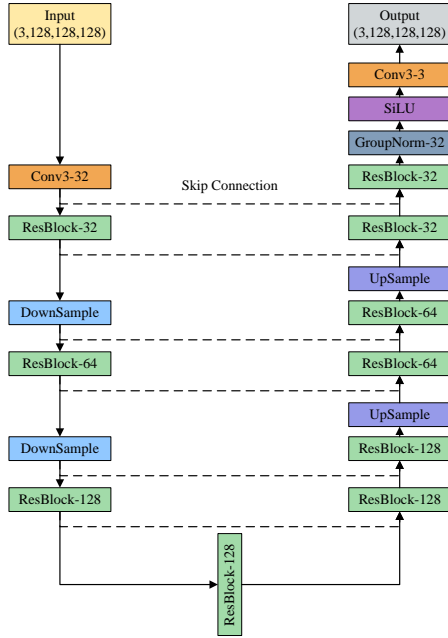


Figure L: Our vertex refiner (U-Net) for 128 resolution.

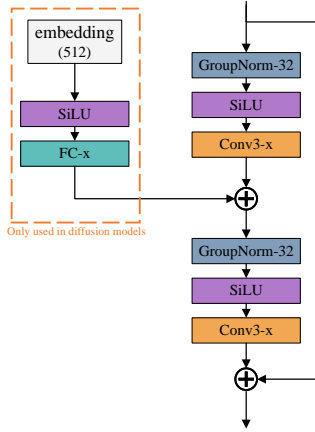


Figure M: The architecture of our ResNet Block.

similarity between two point clouds:

$$EMD(A, B) = \min_{\phi: A \rightarrow B} \sum_{a \in A} \|a - \phi(a)\|_2, \quad (18)$$

where ϕ is the bijection between A and B .

Light field descriptor (LFD) [6, 9, 26] utilize silhouette images rendered from 20 camera poses to measure the structure similarity between two shapes.

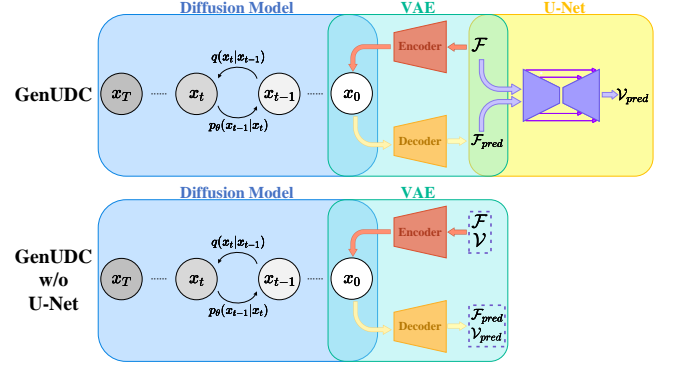


Figure N: The pipeline differences between GenUDC and GenUDC without U-Net.

Jensen-shannon divergence (JSD) is calculated between two marginal point distribution of A and B :

$$JSD(P_X, P_Y) = \frac{1}{2} D_{KL}(P_X || M) + \frac{1}{2} D_{KL}(P_Y || M), \quad (19)$$

where P_X and P_Y are marginal distributions of points in the generated point clouds A and the reference point clouds B respectively. To approximate, we discretize the point cloud space into 28^3 voxels and assign each point to one of P_X and P_Y .

Coverage (COV) measures the diversity of generated dataset X in comparison to the reference dataset Y . For each $x \in X$, it finds a nearest neighbor $y \in Y$ as a match. COV is the fraction of matched y in the reference dataset Y :

$$COV(X, Y) = \frac{|\{ \arg \min_{y \in Y} D(x, y) | x \in X \}|}{|Y|}, \quad (20)$$

where $D(\cdot, \cdot)$ is a distance function, such as CD, EMD, or LFD.

Minimum matching distance (MMD) measures the quality of X referred to Y . For each $y \in Y$, it finds the nearest neighbor x in X and records $D(x, y)$. MMD is the mean of those distances:

$$MMD(X, Y) = \frac{1}{|Y|} \sum_{y \in Y} \arg \min_{x \in X} D(x, y) \quad (21)$$

1-nearest neighbor accuracy (1-NNA) [43] measures the similarity between two distributions:

$$1-NNA(X, Y) = \frac{\sum_{x \in X} \mathbb{I}(n_x \in X)}{|X| + |Y|} + \frac{\sum_{y \in Y} \mathbb{I}(n_y \in Y)}{|X| + |Y|}, \quad (22)$$

where n_x is the nearest neighbor of x in $X \cup Y - \{x\}$ and $\mathbb{I}(\cdot)$ is an indicator function. For example, if $n_x \in X$, $\mathbb{I}(n_x \in X) = 1$. If $n_x \notin X$, $\mathbb{I}(n_x \in X) = 0$. Ideally, if X and Y are sampled from the same distribution, the 1-NNA value should be 50%. The closer the 1-NNA value is to 50%, the more similar X and Y are.

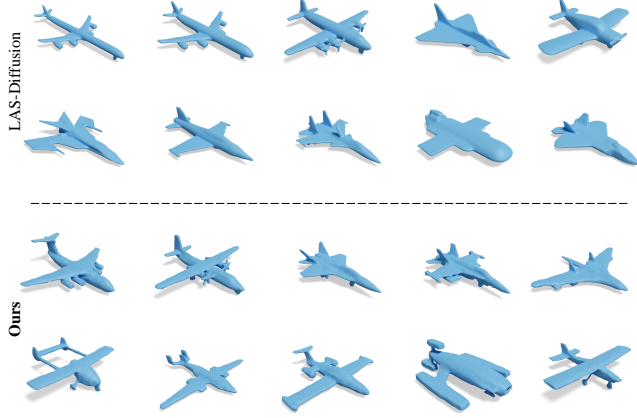


Figure O: Qualitative evaluation of shape generation in 128^3 resolution.

D GenUDC without U-Net

We present the pipeline of GenUDC without U-Net in Fig. N. In GenUDC without U-Net, we remove the vertex refiner (U-Net) and concatenate the face part \mathcal{F} and the vertex part \mathcal{V} together to train the latent diffusion model.

E More Visual Samples of GenUDC

We present visual samples of 128 resolution in Fig. O. Both methods are visually good. It is difficult to distinguish which method is better according to those visual samples. However, Tab. 3 of the main paper proves that our variety and distribution are better than LAS-Diffusion [78].